physica status solidi b
www.pss-b.com

Quantum Transport in Nanostructures of 3D Topological Insulators

*Romain Giraud and Joseph Dufouleur**

Quantum transport measurement is an efficient tool to unveil properties of topological surface states in 3D topological insulators. Herein, experimental and theoretical results are reviewed, presenting first some methods for the growth of nanostructures. The effect of the disorder and the band bending is discussed in details both experimentally and theoretically. Then, the focus is put on disorder and quantum confinement effect in topological surface states of 3D topological insulators narrow nanostructures. Such effect can be revealed by investigating quantum interferences at very low temperature such as Aharonov–Bohm oscillations or universal conductance fluctuations.

1. Introduction

In the last 15 years, Z_2 topological insulators (TIs) were identified as new topological states of matter and were intensively studied both theoretically and experimentally (see, for instance, refs. [1–3] for early reviews and ref. [4] for a review focusing on transport). Many TIs are small-gap semiconductors, for which the spin–orbit coupling is strong enough to induce a band inversion, such that the bulk energy gap closes at the interface with any conventional insulator. It results in the formation of gapless electronic states, which host Dirac fermions propagating at edges or surfaces, depending on the TI dimensionality (2D or 3D, respectively). Because of the strong spin–orbit coupling and time-reversal symmetry (TRS), these electronic states have a specific spin texture, with a reversed chirality for opposite interfaces, and therefore a band structure made of spin-helical Dirac fermions. Theory predicts that the existence of topological surface states (TSS) in 3D TIs is topologically protected by TRS. Thus, these gapless states are robust against any kind of nonmagnetic disorder, and direct backscattering is forbidden by the spin texture.[1] Such new properties have direct consequences on the quantum transport of Dirac fermions, showing a very rich physics that can be revealed in simple geometries of mesoscopic conductors such as nanowires (NWs) or nanoribbons.[4–20]

The suppression of backscattering leads to the ballistic motion of charge carriers in 2D TIs, in the so-called quantum spin Hall state. This was predicted for HgCdTe heterostructures,[21,22] and experiments unambiguously evidenced the nontrivial topology of the 2D band structure.[23] However, to reveal the topological transport properties in 3D TIs remained a very challenging task, in particular if the Fermi energy is pinned far away from the Dirac point. Indeed, the backscattering of 2D topological surface states is restored by a static disorder through multiple-scattering processes, which results in a finite transport length, restricting quasi-ballistic transport to narrow nanostructures. It is nevertheless possible to get some indirect indications of the nontrivial topology of the band structure by revealing other specific properties of TSS in 3D topological insulators such as the spin polarization of the band structure (combining, for instance, transport and optics[24]) and the related anisotropic scattering[14] or the linear dispersion of quasiparticles.[17,25]

In many cases, another intrinsic limitation came from the finite bulk-carrier conductivity, often dominating the conductance in 3D TI films. An elegant way to overcome this issue and to evidence the existence of TSS was found by studying quantum coherent transport in 3D TI NWs and revealing their contribution to well-defined Aharonov–Bohm oscillations of the magnetoresistance, by applying a magnetic field along the axis of the nanostructure.[5] Aharonov–Bohm oscillations are directly related to the quantum confinement of surface Dirac fermions in the NW cross section, thus leading to a flux-tunable quantized band structure that strongly differs from that of bulk carriers, and quantum transport measurements indeed became a powerful tool to investigate the specific physics of TSS in 3D TI quantum wires. In such nanostructures, all surface modes lose their topological protection, but for one mode that becomes gapless if half of a flux quantum is applied.[4] Therefore, in a NW geometry, all modes are partially reflected at the interface between

Dr. R. Giraud, Dr. J. Dufouleur
Leibniz Institute for Solid State and Materials Research
IFW Dresden
P.O. Box 270116, D-01171 Dresden, Germany
E-mail: j.dufouleur@ifw-dresden.de

Dr. R. Giraud
CEA
Spintec
CNRS
University of Grenoble Alpes
F-38000 Grenoble, France

Dr. J. Dufouleur
Center for Transport and Devices
TU Dresden
D-01069 Dresden, Germany

The ORCID identification number(s) for the author(s) of this article can be found under https://doi.org/10.1002/pssb.202000066.

DOI: 10.1002/pssb.202000066

the contact and the NW, as a result of both the disorder and the wave vector mismatch, except for the zero energy mode, which is a perfectly transmitted mode (PTM).[19] This spin-helical topological mode is reminiscent of the quantum spin Hall edge states. Its measurement, even in the presence of a strong disorder (when all other modes are not transmitted anymore), would be an unambiguous hallmark of the nontrivial topology of the system.[7] Beyond these unusual transport properties, a 3D TI NW contacted with metallic leads presents many more thrilling properties when contacted to superconducting leads. Indeed, the PTM connected by s-wave superconducting contacts hosts Majorana fermions, so that the PTM could be evidenced by measuring the dependence of the supercurrent with an Aharonov–Bohm flux.[26] Yet, the contribution of this topological mode to the surface conductance can only be clearly evidenced if quantum confinement is strong enough (narrow NWs) or if the Fermi energy is low enough, as compared with the transverse energy quantization Δ, so as to have surface transport determined by a small number of transverse modes only.

In most cases however, due to the strong intrinsic doping of 3D TIs, the Fermi energy in real systems usually lies far from the Dirac point which prevents any observation of unambiguous nontrivial topological features despite some promising results.[12,13,15] Nevertheless, even at high energies and for a rather large number of transverse channels, 3D TI quantum wires still exhibit unusual characteristics like a strongly reduced backscattering[11,14] and an insensitivity to the disorder's strength[19] or the linear dispersion that could be revealed by the careful measurements and analysis of quantum interferences like Aharonov–Bohm oscillations[11] and universal conductance fluctuations.[17]

In this context, we have considered two different strategies for the growth of 3D TI nanostructures, and investigated the magnetotransport properties of individual nanostructures, such as large flakes, wide nanoribbons, or narrow NWs. First, high-quality single-crystalline nanostructures of Bi_2Se_3 and Bi_2Te_3 were obtained by vapor transport without catalysts.[27] Second, ultra-narrow nanostructures were prepared by electrochemical deposition, with the goal to increase the confinement energy to deplete the bulk by charge transfer effect and to limit the number of transverse modes.[28]

2. Growth of Nanostructures

2.1. Vapor Transport Growth

The growth of nanostructures of 3D TIs is a key issue for the investigation of the transport properties of TSS. As most of the 3D TIs are van der Waals materials, the first method used to contact and measure thin films of 3D TIs was the exfoliation technique, following the processes developed for graphene samples. This method has the advantage of using macroscopic crystals, which growth is easier for ternary or quaternary compounds, and which allows for precisely adjusting the doping composition. It is therefore possible to chemically tune the position of the Fermi energy in order to deplete the bulk. Nevertheless, the process mechanically damages the crystals and the quality of the surface is not as high as for cleaved crystals.

Romain Giraud is an experimentalist having expertise in nanomagnetism and nanoelectronics. His research first considered quantum magnetism and diluted magnetic semiconductors. Since 2004, he is a CNRS researcher CEA/DRF/IRIG/DEPHY/SPINTEC, Grenoble, France, studying spin and charge transport in nanostructures and novel electronic states at interfaces (2D electron states, topological insulators). After a secondment at the IFW Dresden, Germany (2010–2016), working on 3D topological insulator quantum wires, he joined the CEA/SPINTEC to investigate novel properties related to topology and magnetism, and is responsible for the International Research Projet «SPINMAT» between SPINTEC and the IFW.

Joseph Dufouleur studied physics at the University of Paris-Sud and engineering in Supélec (Paris, France). He got his Ph.D. in the group of Dominique Mailly on quantum transport in 2D electron gas. Subsequently, he worked in the nanoelectronic group of Christian Glattli at CEA/SPEC and in the group of Prof. Anna Fontcuberta i Morral at the Walter Schottky Institute (TUM, Munich, Germany). In 2011, he joined the IFW Dresden where he set up together with Romain Giraud a quantum transport group.

To have some high-quality crystals and surfaces, we developed a new process to optimize the growth of Bi_2Se_3 nanostructures by catalyst-free decomposition sublimation in sealed silica ampoule (see **Figure 1**). It shows a couple of advantages when compared to techniques (electrodeposition, molecular beam epitaxy)[27]: 1) high-quality single-crystalline nanostructures can be obtained with atomically flat facets; 2) different shapes of the nanostructures can be prepared with a tape-free method (large nanoflakes, long NWs, or nanoribbons) and with no need of additional etching; 3) the nanostructures' thicknesses can be as small as a few nm; and 4) there is no contamination from a catalyst.

Nanostructures are directly grown on SiO_2/Si^{++} substrates by a vapor–solid growth mechanism. We used sealed silica ampoules with a source zone with Bi_2Se_3 powder and a sink zone with the SiO_2/Si^{++} wafer. The ampoules are placed in a furnace with a temperature profile such that the hot part coincides with the source zone at a temperature close to the decomposition temperature ($T_2 = 500$–$600\,^{\circ}C$). The sink zone is at a lower temperature ($T_1 = 430$–$460\,^{\circ}C$). The Bi_2Se_3 powder at the hot spot is sublimated in BiSe and Se_2 gases which diffuse and recrystallize in the sink zone. Such a growth makes it possible to obtain crystals with a high degree of crystallinity and nanostructures up to few μm long and down to few tens of nm thick. The high quality of as-grown nanostructures was confirmed by transmission electron microscopy including selected area electron diffraction as well as by electrical transport measurements.[27] Recently,

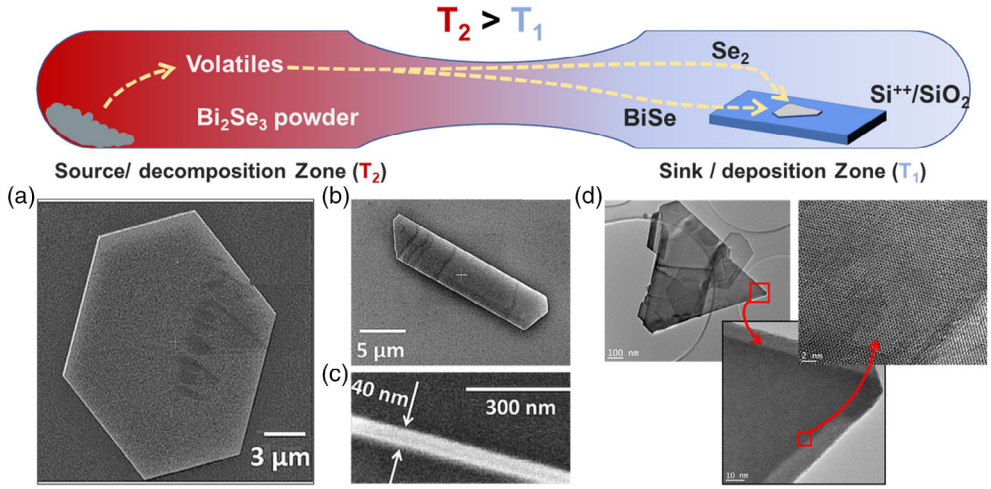

Figure 1. Schematic of the principle of the vapor transport growth for Bi_2Se_3. The growth could be adapted to grow different binary compounds like Bi_2Te_3 or WTe_2, according to the same principle as for Bi_2Se_3. We obtained few nanometer thick as-grown a) nanoflakes, b) nanoribbons, and c) NWs, with a d) high crystal quality. Adapted with permission.[27] Copyright 2015, American Chemical Society.

this approach was successfully adapted to the growth of Bi_2Te_3 and WTe_2 nanostructures.

2.2. Electrochemical Deposition

For the study of quantum confined systems, another growth strategy can be followed to grow 3D TI NWs suitable for the investigation of quantum confined systems by focusing on the strength of the confinement energy Δ instead of tuning the Fermi energy in the gap. As $\Delta = h v_F / L$ with h the Planck constant, v_F the Fermi velocity, and L the perimeter of the NW, this method consists in developing the growth of NWs with diameters L as small as possible. This leads therefore to a reduction of both the bulk-to-surface ratio and, importantly, of the number of transverse modes.

The electrochemical deposition of 3D TI NWs within ion-track etched polymer membranes might be in this view a suitable growth method.[29–31] The principle of such a growth is shown in **Figure 2** together with some TEM pictures of NWs grown by this technique. NWs of Bi_2Te_3 with diameters ranging from 25 to 120 nm could be obtained. The relatively poor crystal quality of the NWs is not an issue for the transport study of topological insulators and might be even an advantage because the disorder limits the transmission of the different transverse mode except the one of the perfectly transmitted mode that is fixed to 1 by the nontrivial topology.[19] Therefore, the use of disordered quantum confined structures naturally increases the contribution of the topological mode over the trivial modes. Nevertheless, the relatively strong doping of the NWs remains a limitation of this growth technique.

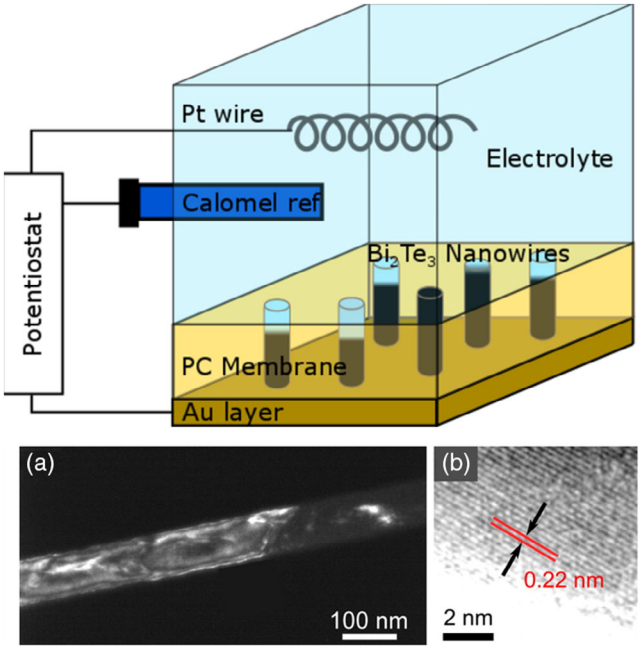

Figure 2. Schematics of the electrochemical deposition of Bi_2Te_3 NWs within ion-track etched polymer membranes. a) Dark-field TEM image of a representative 100 nm diameter NW. b) High-resolution TEM image of a single-crystalline section of a NW. The atomic planes parallel to the wire axis exhibit an interplanar distance of about 0.22 nm. Adapted with permission.[31] Copyright 2016, American Chemical Society.

3. Transport Properties of 2D Surface States

3.1. Band Bending

As a consequence of the presence of surface states, a band bending occurs in the bulk of 3D TIs, close to the interface with a trivial insulator. This band bending is generally upward because the surface states have to be filled with some extra charges. Therefore, in an n-doped bulk, the density of charge is lower at the vicinity of the surface states over a length scale given by the Thomas–Fermi screening length λ_{TF} ($\approx$ a few nm)[14,32] and a depletion region might even appear in low doped structures. Using this band bending effect is a very efficient way to deplete very thin flakes of 3D TIs (see, for instance, ref. [9]).

The measurements of Shubnikov–de Haas oscillations in 3D TI flakes or nanoribbons are a convenient way to investigate quantitatively the band bending, provided that all contributions (lower surface states, upper surface states, and bulk states) can be resolved and attributed correctly. The onset of the Shubnikov–de Haas oscillations being roughly set by the relation $\mu B = \omega_c \tau_Q \gtrsim 1$ with μ the mobility, $\omega_c = eB/m^*$ the cyclotron frequency, τ_Q the quantum lifetime of the quasiparticles, B the magnetic field and m^* the effective mass require the measurements to be of high-quality structure (larger μ) or measuring under very high magnetic field.

The band bending in different structures of Bi_2Se_3 was systematically studied at low temperature and under high magnetic field (B up to 55 T) in ref. [32]. Using the gate dependence of the oscillations and considering the effective mass extracted from the temperature dependence of the Shubnikov–de Haas oscillations, it was possible to assign the different frequencies of the oscillations to the different charge carriers populations (see **Figure 3**). This allows for the determination of the band bending in 3D TIs nanostructures with bulk charge density n_b ranging from $n_b = 2.6 \times 10^{19}\,cm^{-3}$ down to $n_b = 6.6 \times 10^{17}\,cm^{-3}$.

For highly doped samples (about $10^{19}\,cm^{-3}$), an upward band bending of 35 meV up to 150 meV is observed. The difference between the amplitudes of the band bending is essentially given by the type of the interface: with vacuum (or equivalent) or with the substrate. The large difference between the two types of interface probably comes from some doping that limits the band bending on the upper surface states.

Importantly, the low doped structure ($n_b = 6.6 \times 10^{17}\,cm^{-3}$) shows a very strong downward band bending (down to −260 meV). Such a strong effect even induces the formation of two additional 2D electron gases contributing in parallel with the nontrivial surface states. Those surface states are the results of the quantization of the perpendicular wave vector of the bulk charge carriers close to the surface. They have a trivial origin and host massive charge carriers. Such a downward band bending points therefore at the necessity of controlling both the residual bulk doping and the additional surface/interface doping to produce bulk-compensated structures. In particular, the very strong downward band bending near the interface with the substrate suggests that the interface with SiO_2 favors in some cases a strong interface doping, which could result either from a locally increased disorder in Bi_2Se_3 or from chemical bonds.

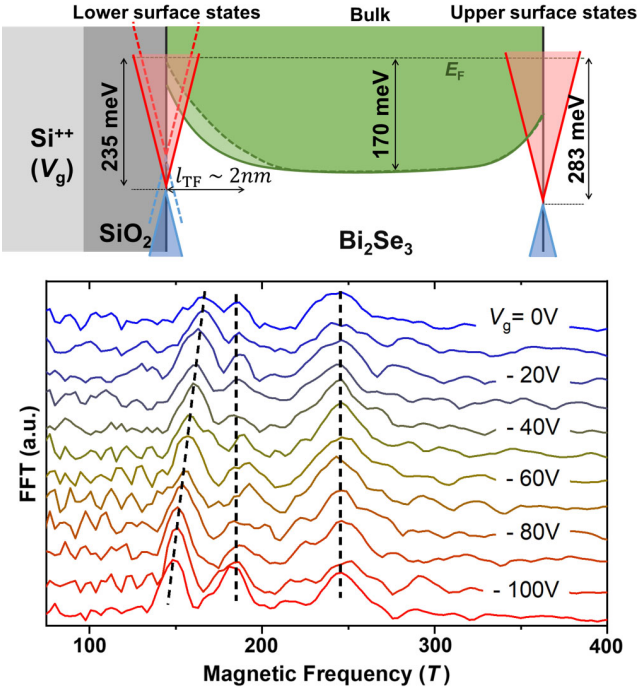

Figure 3. Band structure of a Bi_2Se_3 nanoribbon with the band bending measured close to the upper and lower surface states and the relative change of the band structure when a gate voltage is applied on the back-gate. The gate dependence of the Fourier transform of the Shubnikov–de Haas oscillations in the Bi_2Se_3 nanoribbon is shown below. Three different peaks can be clearly observed. Based on their gate dependence and on considerations of the effective mass, they could be assigned to the different charge carriers (upper and lower surface states as well as bulk states). Adapted with permission.[14] Copyright 2016, American Chemical Society.

3.2. Scattering Anisotropy

A hallmark of 2D topological insulators is the suppression of backscattering in edge states and a ballistic transport of the charge carriers over long length scales.[23] The forbidden backscattering is the result of the spin polarization of the edge states and the spatial split between the forward and backward edge states for a given spin. In 3D TIs, the strong spin–orbit coupling implies a spin-momentum locking in topological surface states which results in a forbidden backscattering as in the 2D case. Nevertheless, contrarily to the 2D case, other scattering angles are allowed and the backscattering is restored through multiple scattering processes (see **Figure 4**). Therefore, the spin polarization of the topological surface state's band structure does not result in a ballistic motion of the charge carriers but rather favors forward scattering over backward scattering and, therefore, enhances the mobility. Generally, the enhancement of the

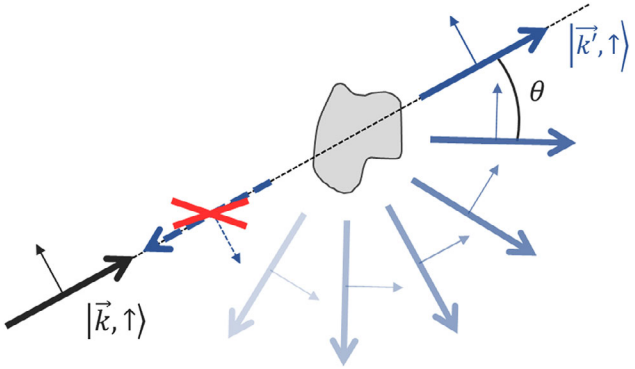

Figure 4. An incident state with wave momentum **k** is scattered in a state with a wavevector **k**′ in a topological surface state with an angle θ between the intial and the final state. All scattering angles except the backscattering angle are allowed in a 2D topological surface states, but the spin polarization of the band structure favors forward scattering. Adapted with permission.[14] Copyright 2016, American Chemical Society.

mobility due to the spin polarization of the band structure only is limited to a factor of 2.

The angular dependence of the scattering implies an anisotropic scattering. The spin polarization of the band structure is nevertheless not the only source of anisotropic scattering in transport. A long-range disorder can result, for instance, in a very strong scattering anisotropy.[33–36] To quantitatively understand the different contributions to such an anisotropy, between the band structure origin on the one side (spin polarization) and the nature of the disorder on the other side, it is possible to use some simple and general models as described in refs. [7,19,37].

The Fermi golden rule makes it possible to define two different time scales: the quantum lifetime τ_Q of a particle and the transport time τ_{tr}. τ_Q gives the time scale for a particle to be scattered in any other final state, independently of the direction of the final state, whereas τ_{tr} emphasizes the influence of final states pointing in the backward direction. Both times can be, respectively, written as

$$\frac{1}{\tau_Q} = \frac{2\pi}{\hbar}\sum_{\mathbf{k}'}|\langle\mathbf{k}|W|\mathbf{k}'\rangle|^2\delta(E_{\mathbf{k}} - E_{\mathbf{k}'}) \tag{1}$$

$$\frac{1}{\tau_{tr}} = \frac{2\pi}{\hbar}\sum_{\mathbf{k}'}|\langle\mathbf{k}|W|\mathbf{k}'\rangle|^2(1-\cos\theta)\delta(E_{\mathbf{k}} - E_{\mathbf{k}'}) \tag{2}$$

where W is the disorder potential and θ is the angle between an initial state $\mathbf{k}$ and a scattered state $\mathbf{k}'$ (see Figure 4). The disorder is fully characterized by its correlation function

$$\langle W(\mathbf{r})W(\mathbf{r}')\rangle = g\frac{(\hbar v)^2}{2\pi\xi^2}e^{-|\mathbf{r}-\mathbf{r}'|^2/2\xi^2} \tag{3}$$

where g is the unitless strength of the disorder and ξ is the correlation length of the disorder. We can define the mean free path $l_e = v\tau_Q$ and the transport length $\ell = v\tau_{tr}$ (v is the Fermi velocity) and after some algebra, we find for isotropic topological surface states

$$\frac{l_e}{\xi} = \frac{2}{gk\xi}\frac{\exp(k^2\xi^2)}{I_0(k^2\xi^2) + I_1(k^2\xi^2)} \tag{4}$$

$$\frac{\ell}{\xi} = \frac{2k\xi}{g}\frac{\exp(k^2\xi^2)}{I_1(k^2\xi^2)} \tag{5}$$

where k is the Fermi wavevector and I_n is the modified Bessel function of order n. The dependence of ℓ with $k\xi$ is shown in **Figure 5** where the short- and the long-range disorder regimes can be distinguished by the value of $k\xi$.

In the short-range disorder regime ($k\xi \ll 1$), the transport length diverges due to the vanishing density of states of topological surface states. This is specific to massless fermions because the 2D density of states for massive fermions is constant and ℓ vanishes at low energy. We note that close to zero energy, the approximation made to obtain the equations Equation (5) and (4) is not valid any more and the divergence should be smoothed out.

In the long-range disorder limit ($k\xi \gg 1$), ℓ increases quadratically with $k\xi$ due to the anisotropy of the scattering. As shown schematically in **Figure 6**, this anisotropy of the scattering is not due to a spin polarization of the band structure but rather to the reduction of the angle between the initial $\mathbf{k}$ and the scattered $\mathbf{k}'$

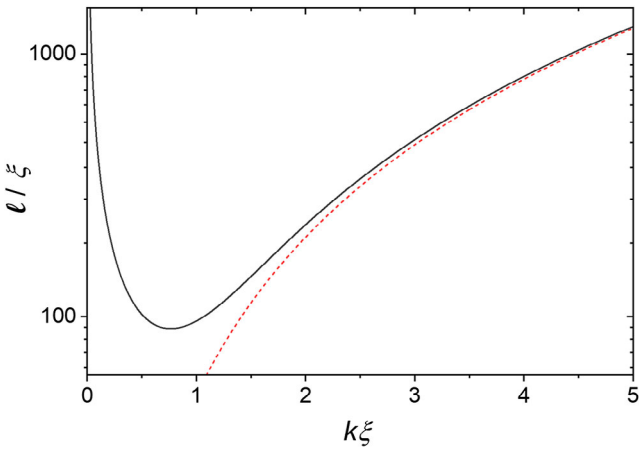

Figure 5. Dependence of ℓ/ξ with $k\xi$ in solid black line for $g = 0.1$. The dashed line is the long-range disorder limit ($k\xi \gg 1$) where $\ell/\xi \propto k^2\xi^2$.

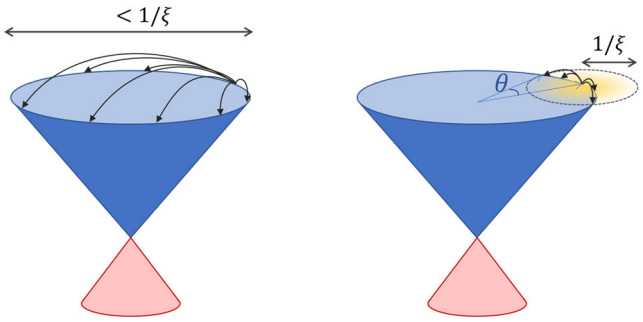

Figure 6. Illustration of an isotropic scattering (left) and anisotropic scattering (right). In the isotropic scattering, all the states at the Fermi energy are equally accessible, whereas the available states are restricted in a small area (in yellow) close to the initial state with a small θ angle for an anisotropic scattering. The cutoff that determine the available state is given by $\approx 1/\xi$.

state (the area in yellow in Figure 6). The area available for a scattered state in the reciprocal space is given by $1/\xi$ and $1/\xi$ which acts as a cutoff for $|\mathbf{k} - \mathbf{k}'|$.

To give some insight into the respective contributions of the spin polarization of the band structure and of the cutoff of the scattering by the disorder, it is usefull to look at the ratio $\tau_{tr}/\tau_Q = \ell/l_e$. Generally, this ratio is a direct measurement of the scattering anisotropy. An isotropic scattering gives $\tau_{tr}/\tau_Q = 1$, whereas a strong anisotropic scattering leads to τ_{tr}/τ_Q that can largely exceed 1. More precisely, in the low $k\xi$ limit, the ratio is equal to two, accounting for the spin polarization of the band structure. For large $k\xi$, the spin polarization has no influence anymore and the ratio is the result of the cutoff due to the long-range nature of the disorder.

This ratio is shown in **Figure 7**. We note that it does not depend on the strength of the disorder g anymore, being therefore a good choice for comparison with experimental data. We also note that a more realistic model taking into account the case of both, point-like impurities and charged impurities was developed in ref. [38] and gives the same trend.

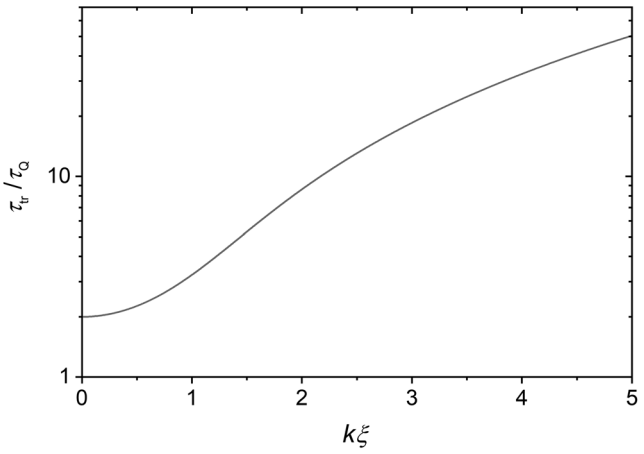

Figure 7. Dependence of the $\tau_{tr}/\tau_Q = \ell/l_e$ ratio in the framework of our model.

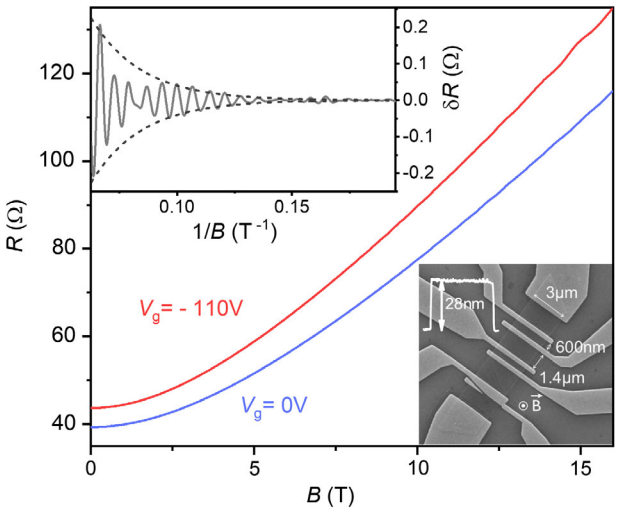

Figure 8. Voltage dependence of the magnetoresistance of the nanoribbon for $V_g = -110$ V and $V_g = 0$ V. Lower inset: SEM picture of the nanoribbon that was measured for the investigation of anisotropic scattering with an atomic force microscopy profile that indicates a height of 28 nm together with an atomically flat surface. Upper inset: observation of tiny Shubnikov–de Haas oscillations in which extrema are fitted by a Dingle plot. Adapted with permission.[14] Copyright 2016, American Chemical Society.

In the low energy regime in Figure 7, the ratio τ_{tr}/τ_Q becomes equal to two. In this regime, the Fermi wavevector is very small and the cutoff due to the disorder does not play any role so that the anisotropy can be entirely attributed to an effect of the spin polarization of the band structure. In the high energy regime, the ratio τ_{tr}/τ_Q diverges. In this regime, the scattering anisotropy is dominated by the cutoff in $|\mathbf{k} - \mathbf{k}'|$ implied by the disorder when $k\xi \gg 1$ and the spin polarization does not play any significant role.

In ref. [14], the scattering anisotropy was measured in a Bi_2Se_3 nanoribbon. In principle, this requires the measurement of τ_{tr} and τ_Q for at least one surface state. Nevertheless, the determination of the two timescales for one surface state is only possible through the determination of all transport parameters, i.e., for the bulk and the two surface states. This was possible in a sample for which some characteristics were already shown in the previous section (see Figure 3). In this nanoribbon, the Fourier transform of the Shubnikov–de Haas oscillations reveals three peaks induced by the bulk states as well as the upper and lower surface states. The gate dependence of the oscillations allows for attributing the low-frequency peak to the lower surface states. The temperature dependence of the Shubnikov–de Haas oscillations makes possible the determination of the effective mass for different extrema, which results in the attribution of the intermediate peak to the bulk states and the high-frequency peak to the upper surface states (see ref. [14]). The three peaks being very well separated at a gate voltage $V_g = -110$ V, it was possible to filter each of them and to fit the extrema by a Dingle plot to get the quantum lifetime or, equivalently, the mean free path l_e for each charge carrier type (see **Figure 8**). It gives $l_e = 21$ nm for the bulk and $l_e = 28$ nm for the two surface states. Such similar values indicate that the disorder is dominated by a uniform bulk disorder.

Knowing the different charge densities and the mean free paths of the different charge carriers, it is possible to determine the transport lengths ℓ using the gate sensitivity of the conductance and fitting the transconductance of the sample. Assuming that the disorder is dominated by bulk charged impurities for the two surface states, the transport lengths depend on the charge density[38] and the difference between the two surface states transport lengths is the result of the different charge densities between the lower and upper surfaces only. A transport length of 28 nm was found for the bulk and a significantly larger transport length was found for the two surface states (about 200 nm for both surface states). This value could be confirmed in an independent way by measuring universal conductance fluctuations, as shown in ref. [14].

Despite a common disorder, the determination of the ℓ/l_e ratios could evidence an isotropic scattering in the bulk ($\ell/l_e = 1.3$) and a significant anisotropic scattering in the topological surface states ($\ell/l_e = 7.0$ and 8.4 for the lower and upper surface states, respectively). The anisotropy of the scattering measured in the topological surface states has two different origins. The first one is the spin polarization of the band structure that contributes to enhance the ratio up to a factor 2. The second one is the spatial distance between the charged impurities of the disorder and the surface states. This spatial distance leads to a smoothing of the disorder potential which results in an enhancement of the correlation length[38] and, therefore, of the anisotropy and its related ℓ/l_e ratio.

A consequence of the significantly larger transport length of the surface states with respect to the bulk transport length is the large contribution of the surface states to the conductance (about 55% of the total conductance), even for a thickness (≈28 nm) that is much above the depletion length (few nm). Importantly, as the transport length ℓ is also the spin-relaxation length in TSS (due to the spin-momentum locking[39]), the large transport length measured in topological surface states opens the way to the development of spintronics devices and confirms the high potential of 3D TI-based spintronics. Moreover, this large transport length makes the realization of quantum confined 3D TI systems possible, as described later.

4. Transport in Quantum Confined Topological Insulators

The investigation of quantum confined 3D TI systems is a promising way for unveiling the nontrivial topology of the band structure of 3D TIs. It consists in the confinement of the surface states to one dimension (3D TI NWs) or zero dimension (3D TI quantum dots). In the following, we will take interest in the transport properties of NWs. A NW will be quantum confined as soon as its transport length is longer than or of the same order of magnitude as its diameter L ($\ell \gtrsim L$). As soon as this condition is satisfied, the description of the system in terms of (almost) independent transverse channels becomes suitable for understanding the transport properties of the system.

In a NW geometry, the periodic boundary conditions result in a quantization of $k_\perp$, the perpendicular component of the wave vector $\mathbf{k} = (k_\perp, k_\parallel)$. We have $k_\perp = k_n = \varepsilon_n/\hbar v = (n + \phi/\phi_0 - 1/2) \times \Delta/\hbar v$ where the offset 1/2 comes from the Berry phase, $n \in \mathbb{Z}$ is a mode index, ϕ is the magnetic flux threaded through the cross section of the NW, $\phi_0 = h/e$ is the magnetic flux quantum, and ε_n is the transverse energy of the mode n. The band structure of the NW corresponds therefore to the 2D band structures without any quantum confinement and cut at specific values of the transverse vector $k_\perp = k_n$, each cut corresponding to a transverse mode. If we neglect Zeeman coupling, the presence of a magnetic field aligned along the axis of the NW will only shift the position of the different cuts as shown in **Figure 9**a. Generally, due to the presence of a magnetic field, the band structure is not time reversal symmetric. In other words, for a nonzero value of the magnetic field, if $|\mathbf{k}, \mathbf{s}\rangle$ is an eigenstate of the system, there is no reason for the time reversal symmetric state $|-\mathbf{k}, -\mathbf{s}\rangle$ to be an eigenstate. Nevertheless, we note two singular cases for $\phi = n\phi_0$ or $\phi = (n + 1/2)\phi_0$, for which the band structure is again time reversal symmetric (see Figure 9b).

In the case of nondisordered NWs, the different tranverse channels are not coupled together and the knowledge of the transmission T_n of all channels gives access to all the transport properties (conductance, shot-noise, or any higher order moment of the conductance). The presence of a disorder induces intermode scattering and for a strong disorder, the description of the system in terms of independent channels fails to describe the transport properties. Importantly, the zero energy mode ($n = 0$) has very similar properties to the edge states of a 2D TI: when half a quantum of flux is threaded through the NW, the only way for a charge carrier to be backscattered in the same channel (keeping $k_\perp = 0$ and reversing $k_\parallel$) is to flip its spin. Therefore, backscattering is forbidden as long as time reversal symmetry holds and this mode should be perfectly transmitted as the edge states of a 2D TI.[7] The existence of such PTM is related to the odd number of transverse channels for $\phi = \phi_0/2$.[40] It is therefore not limited to the weak disorder case, and it is expected to persist even in strongly disordered systems.[19]

4.1. Aharnov–Bohm Interferences in Confined and Disordered 3D Topological Insulator NWs

To probe the properties of the PTM, one needs NWs with no conduction through the bulk and a Fermi energy that lies close to the Dirac point. These conditions are rarely found in realistic systems for which the gate effect is usually weak and the Fermi energy relatively high such that many channels contribute to the conductance. This prevents the investigation of the PTM. Nevertheless, even at high energy, disordered 3D TI NWs have some very unusual properties that can be experimentally probed.

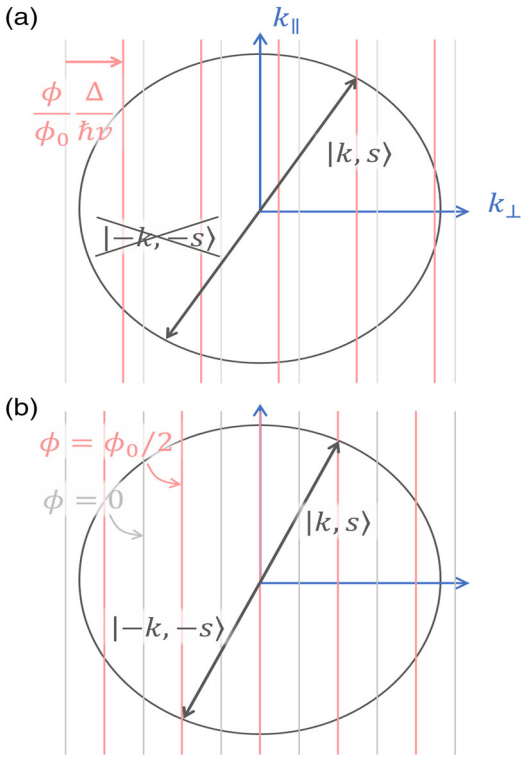

Figure 9. a) Band structure of a 3D TI NW embedded in a magnetic field oriented along the axis of the NW. Without any magnetic field, the band structure of the quantum confined system corresponds to some cut in the Fermi circle at discrete values k_n of the transverse wave vector (gray lines). With a magnetic field, the position of the cut is shifted by a quantity proportional to the magnetic field flux through the cross section of the NW (red lines). As a result, if $|\mathbf{k}, \mathbf{s}\rangle$ is an eigenstate of the system, $|-\mathbf{k}, -\mathbf{s}\rangle$ will not be necessary eigenstate as well. b) When $\phi = n\phi_0$ (gray lines) or $\phi = (n + 1/2)\phi_0$ (red lines), the band structure is time reversal symmetric. The latter case corresponds to the emregence of a perfectly transmitted mode.

For a NW contacted with metallic contact as considered in ref. [7], reflections occur at the interface between the contact and the NW due to the mismatch of the $k_\parallel$, the component of the $\mathbf{k}$ vector parallel to the axis of the NW. The NW is therefore a Fabry–Pérot resonator in which resonances can be averaged out for long NWs. For ideal contacts, we found that[19]

$$\langle T_n \rangle = \sqrt{1 - \left(\frac{\varepsilon_n}{\varepsilon}\right)^2} \tag{6}$$

This transmission is the transmission of a nondisordered NW. A disorder described by the Equation (3) can be introduced in the model and numerical simulations can be

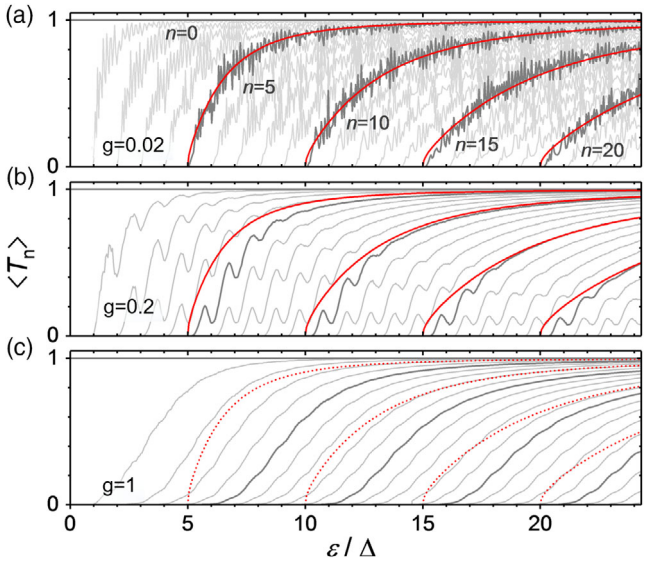

Figure 10. The transmission of the transverse modes calculated and disorder-averaged for different disorder strengths g (0.02, 0.2, and 1) ranging from the ballistic to the diffusive regime. Red lines are the best fit of the transmission including quantum corrections for (a). Good agreement with numerical data is obtained in (b), whereas no satisfactory parameters fit the $g = 1$ data in (c). Reproduced with permission.[19] Copyright 2018, American Physical Society.

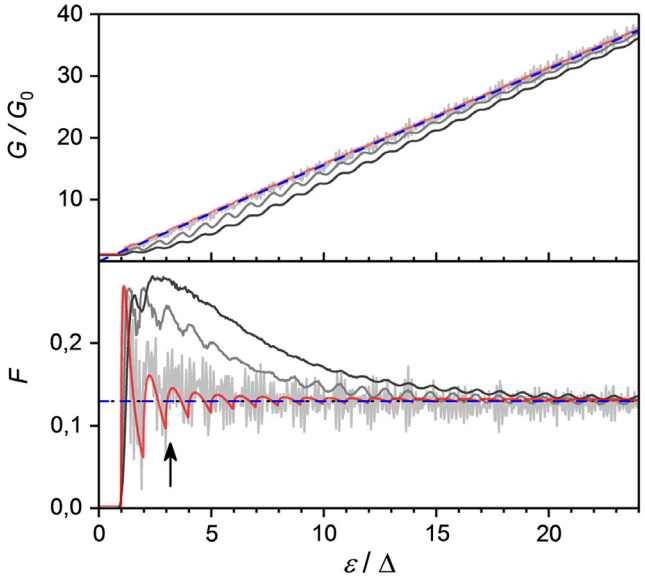

Figure 11. Upper panel: Energy dependence of the conductance. Gray lines are numerical data for $g = 0.02$, 0.2, and 0.5 (from light to dark gray). The red line is the conductance calculated from the T_n including quantum corrections and blue dashed line is the large number of mode limit of Equation (7). Lower panel: Energy dependence of the Fano factor shown with the same color code as for the conductance. The ballistic limit of Equation (8) is shown in blue and the arrow points at the energy corresponding to $k\xi = 1$. Reproduced with permission.[19] Copyright 2018, American Physical Society.

performed to calculate the transmission of the transverse channels, as shown in **Figure 10**. For a weak disorder (top graph in Figure 10), the Fabry–Pérot oscillations are averaged out and the transmission of each mode fits reasonnably with the nondisordered system. Small correction to Equation (6) is nevertheless introduced to account for the residual coupling between transverse modes. For an intermediate disorder (middle graph in Figure 10), good agreement with the simulations could be found far from the onset of each mode but, close to the onset, dips of the transmission appear due to the onset of successive modes associated to the divergence of the 1D density of states. When the dips overlap (lower graph Figure 10), the transmission strongly deviates from the nondisordered transmission and the Equation (6) is not valid anymore, even including quantum corrections.

As already mentioned, it is possible to caclculate the conductance $G = e^2/h \times \sum_i \langle T_i \rangle$ and the Fano factor $F = \sum_i \langle T_i \rangle (1 - \langle T_i \rangle) / \sum_i \langle T_i \rangle$ knowing the transmissions T_i of the different transverse modes. We found

$$G \simeq \frac{e^2}{h} \frac{2\varepsilon}{\Delta} \frac{\pi}{4} \tag{7}$$

$$F \simeq 1 - \frac{8}{3\pi} \tag{8}$$

These expressions are valid only for the nondisordered (ballistic) case. A comparison of this analytical formula with the numerical simulations shows indeed a very good agreement with the low disordered case (see **Figure 11**). Interestingly, a very good agreement in the high energy limit is found even for strongly disordered systems (g up to 0.5). A substantial deviation for strong disorder is observed only when $k\xi \sim 1$ (the arrow in Figure 11). As a result, the transport properties of 3D TI quantum confined systems do not depend on the disorder strength as long as the disorder is long range. The conductance is then proportionnal to the Fermi energy (as in graphene nanoribbons[41,42]) and can be described by a multichannel system with a mean transmission of $\pi/4$. The Fano factor becomes constant and is given by Equation (8).

From such a model, it is also possible to determine the Aharonov–Bohm oscillations in the zero temperature limit and assuming no intermode scattering. The results are shown in **Figure 12**. We see that the oscillations are maximized only at very low energy, when the Fermi energy is very close to the Dirac point such that at most a single mode participates to the transport. Their origin is related to the presence of a PTM when $\phi/\phi_0 = 1/2$ and they can be then as high as e^2/h. Importantly, a π-phase shift is observed every time 2ε takes integer values of Δ. Such phase shifts can be observed even at very high energy, where the PTM does not play any role. It is due to the quantum confinement and to the low coupling of the transverse mode and it has a trivial origin. Such a phase shift was experimentally observed in ref. [15]. We note that taking into account intermode scattering should result first in an increase in the amplitude of the Aharonov–Bohm oscillations which vanish as soon as the dips overlap. The interplay between the disorder and the perfectly transmitted mode was further investigated in ref. [16].

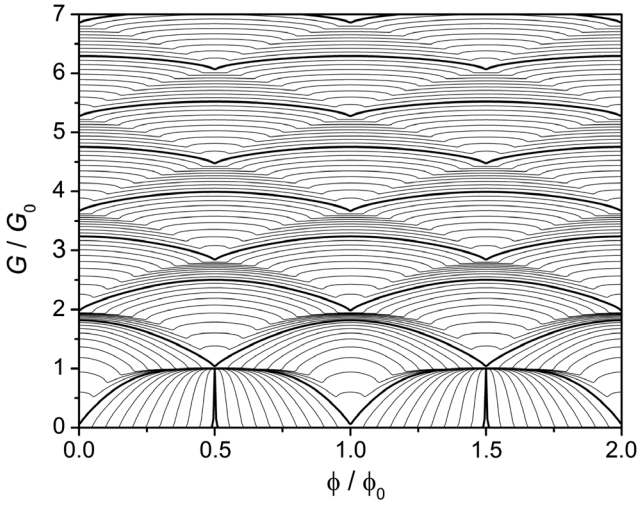

Figure 12. The flux dependence of the conductance (with quantum corrections) for different energy, at a temperature T corresponding to $4k_BT/\Delta = 0.01$ and for $g = 0.02$. The smallest value of the conductance $G(\phi)$ corresponds to $\varepsilon/\Delta = 0$ and the largest one to $\varepsilon/\Delta = 4.5$ in steps of $\varepsilon/\Delta = 0.05$. Energies such that $2\varepsilon/\Delta \in \mathbb{N}$ are indicated with bold lines. Reproduced with permission.[19] Copyright 2018, American Physical Society.

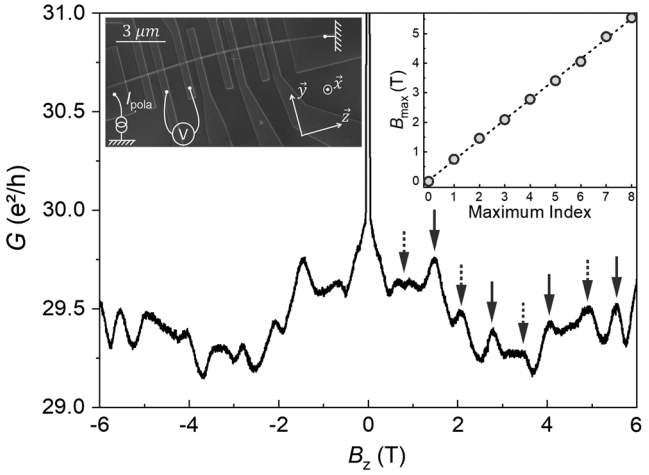

Figure 13. Top left inset: SEM picture of the NW, with a rectangular cross section ($w = 90$ nm, $d = 50$ nm) and a length of about 18 μm. Main panel: Magnetoconductance $G(B_z)$, B_z being parallel to the NW. Dominant periodic oscillations in ϕ_0 are clearly observed (full arrows) and smaller ones in $\phi_0/2$ are also visible (dotted arrows). The top right inset shows the field position of all periodic maxima of the fundamental and first harmonics in the AB oscillations. The linear slope corresponds to $(\phi_0/2)/S$, where S is the effective electrical cross section enclosed by surface states. Adapted with permission.[11] Copyright 2013, American Physical Society.

4.2. Quasiballistic Transport in NWs

Experimentally, the evidence of a quantum confinement in 3D TI nanostructures described in the Section 4.1 was first reported in ref. [11] and confirmed in refs. [12,15,17]. In the pioneer work of ref. [11], the temperature dependence of Aharonov–Bohm oscillations was investigated in a disordered Bi_2Se_3 NW, far from the Dirac point, such that the experimental conditions corresponded to the one presented in the previous section.

In this work, the magnetoresistance of the 3D TI NW at very low temperature ($T = 100$ mK) shows reproducible conductance fluctuations attributed to quantum interferences between electron trajectories. Among aperiodic universal conductance fluctuations, periodic oscillations with a period $\Delta B = \phi_0/S$ ($\phi_0 = h/e$ is the magnetic flux quantum and S is the cross section of the NW) could be evidenced (see **Figure 13**). The cross section S corresponds to surface states buried 5 nm below the surface, a reasonable situation taking into account the oxidation of the surface. Even the first harmonic of the oscillations could be directly observed in the magnetoresistance. In a semiclassical approximation, the oscillations of the nth harmonic correspond to electronic trajectories that encircle at least $n+1$ times the NW, with a phase coherence length L_φ such that $L_\varphi \gtrsim (n+1) \times L$, with L is the perimeter of the NW.

To investigate quantitatively the Aharonov–Bohm oscillations, a careful fast-Fourier transform was performed (**Figure 14**). Up to five harmonics could be evidenced, pointing to the very long L_φ in such systems.

Importantly, the temperature dependence of the different harmonics was studied. All harmonics show an exponential decay with $\delta G_n \propto \exp(-\alpha_n T)$ (see **Figure 15**). In the semiclassical framework, the thermal dependence of the nth harmonic

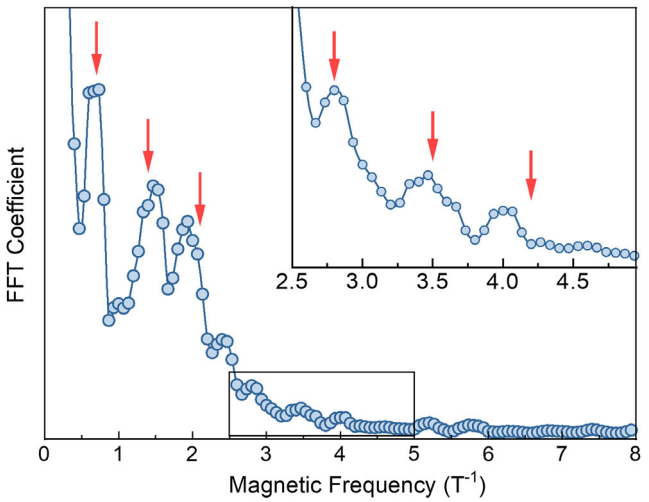

Figure 14. Fast-Fourier transform (FFT) of $G(B_z)$. Vertical red arrows indicate the AB harmonics from the fundamental ($n = 0$) to the highest harmonic observed ($n = 5$). Adapted with permission.[11] Copyright 2013, American Physical Society.

is expected to depend on the phase coherence lenth L_φ like $\exp(-L_n/L_\varphi(T))$, with $L_n = (n+1) \times L$.[43] Therefore, the exponential decay implies that the inverse of phase coherence length has a linear temperature dependence ($L_\varphi \propto 1/T$). This is an unexpected situation for such disordered systems that should be set in a diffusive regime for which $L_\varphi \propto 1/T^{1/3}$.[43] Such a thermal dependence can be found in quasi-1D ballistic systems

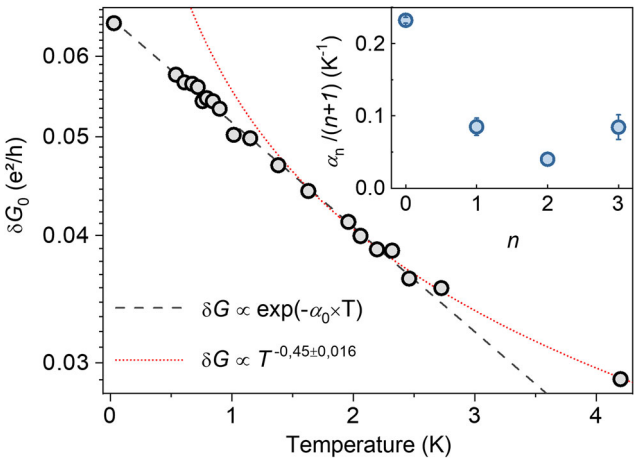

Figure 15. Temperature dependence of the integrated fundamental harmonic, showing a clear exponential decay from 30 mK up to about 2.5 K (open dots: measurement; dashed line: $\exp(-\alpha_0 T)$ fit, excluding the $T = 4.2$ K data point). The high-temperature $1/\sqrt{(T)}$ regime is shown as a dotted line. Higher harmonics follow a similar behavior with a different slope α_n, which do not scale with n (see inset). Adapted with permission.[11] Copyright 2013, American Physical Society.

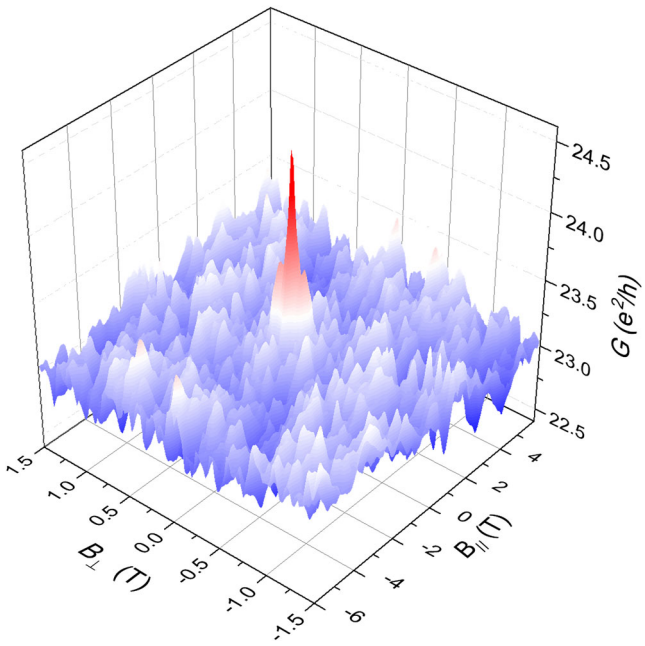

Figure 16. Longitudinal and transverse magnetoconductance $G(B_{\parallel}, B_{\perp})$ of 1 μm-long quantum wire with a perimeter $L = 380$ nm, measured at $T = 100$ mK. Conductance fluctuations due to quantum interferences could be measured both along the axis of the nanoribbon and perpendicular to it with a strong weak antilocalization peak at zero field. Reproduced with permission.[17] Copyright 2017, Nature Publishing Group.

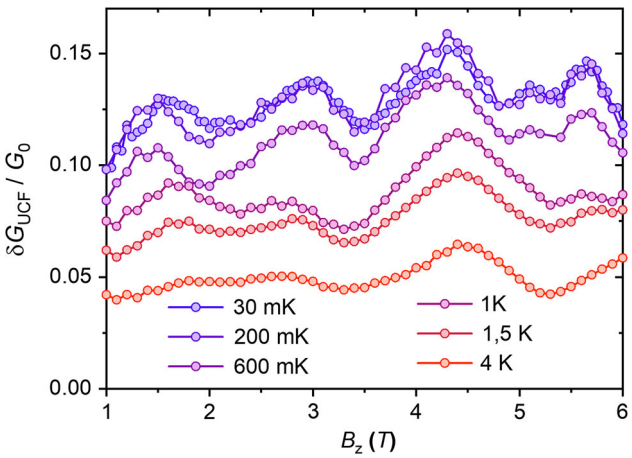

Figure 17. Longitudinal-field dependence of δG_{UCF} measured at different temperatures. A periodic modulation of the conductance fluctuations appears for $T < 1$ K. Reproduced with permission.[17] Copyright 2017, Nature Publishing Group.

with a few number of transverse channels[44] and in the regime of the quantum Hall effect.[45] It indicates that the transport in the transverse direction is ballistic, confirming the quantum confinement of the system in this direction. It remains nevertheless diffusive in the longitudinal direction, setting the system in a quasiballistic regime.

The analysis of the harmonic index "n" dependence of the prefactor α_n in the exponential is found to strongly deviate from linear behavior that could be naively expected from a semiclassical theory (see inset of Figure 15). This is a consequence of the quantum confinement. If the exponential decay for the different harmonics appears to hold in this NW, there is no reason that prefactors α_n preserve their semiclassical expression.

4.3. Universal Conductance Fluctuations in 3D Topological Insulator NWs

Finally, indication of quantum confined surface states could be found even in systems where the Aharonov–Bohm oscillations were not directly observed.[17] Quantum fluctuations were measured in NWs of Bi_2Se_3 and Bi_2Te_3 by sweeping the magnetic field along both the axis of the NW ($B_{\parallel}$ in **Figure 16**) and perpendicular to it ($B_{\perp}$). No evidence was found for periodic Aharonov–Bohm oscillations along the parallel direction. Only aperiodic universal conductance could be measured as well as a strong weak-antilocalization peak at zero magnetic field. Also, the averaged value of the conductance $\langle G(B_{\parallel})\rangle$ along the $B_{\perp}$ sweeps shows an almost constant value and no periodic oscillations was measured.

On the contrary, the amplitude of the fluctuations of the conductance along the $B_{\perp}$ sweeps shows a strong $B_{\parallel}$ dependence (up to 50% at $T = 100$ mK in **Figure 17**) with a periodic modulation. The period corresponds to the introduction of a flux quantum in the cross section of the NWs, which relates this effect to Aharonov–Bohm-like oscillations originating from the surface states.

Such a nonuniversality of the conductance fluctuations is a highly unusual situation in disordered systems with a large number of transverse channels N. Indeed, in the large N limit, even a very weak disorder sets a coherent mesoscopic system in the

universal regime where the conductance fluctuations do not depend on any other parameters (Fermi energy, other magnetic field, disorder strength, geometrical parameters, etc.).

Numerical simulations could nevertheless reproduce experimental results to a reasonable quantitative agreement. The origin of this modulation can thus be attributed to the quantum confinement of Dirac fermions and it provides again a clear indication that we can realize such a quantum confinement even in disordered 3D TIs nanostructures.

5. Conclusion

Many transport properties specific to 3D TI surface states could be probed by quantum transport experiments with single-crystalline nanostructures, confirming the potential of simple devices both for fundamental studies of topological materials and for building spin-based devices, such as NWs for ballistic interconnects, for instance. However, the residual bulk doping due to disorder remains an important limitation. Indeed, in most cases, bulk carriers give a dominant contribution to the total conductance. Moreover, they efficiently screen the electric field induced by a gate, which thus often has only a little influence on the electrochemical potential. For this reason, despite their larger complexity, ternary and quaternary 3D TIs compounds were grown, so as to limit charge transport through the bulk. In ultra-thin nanostructures, the surface-to-bulk conductance ratio even further increases due to the short charge depletion length and the quantum hall effect was evidenced.[46,47] One particularly interesting recent development combined quantum confinement aspects with the growth of partly compensated materials, capped, and contacted in situ to avoid any contamination.[48] The finite density of point defects, that are thermodynamically stable, is, however, present for all growth methods. Ultra-narrow NWs could be therefore good candidates to overcome such remaining issues.

Generally speaking, quantum transport measurements could also be used to investigate novel topological phases that are very promising for spintronics. The discovery of Weyl and Dirac semimetals for instance, or more recently of magnetic topological insulators,[49–52] offers a new platform to create topological states that can be tunable with some external parameters such as small magnetic fields or electrical gates. In these new materials, it is also very important to understand the influence of a static disorder, which may alter some topological properties such as the chiral anomaly.[53]

Acknowledgements

J.D. acknowledges financial support by the Deutsche Forschungsgemeinschaft (DFG) through SPP 1666 Topological Insulators program and the ct.qmat Excellence cluster. Open access funding enabled and organized by Projekt DEAL.

Conflict of Interest

The authors declare no conflict of interest.

Keywords

3D topological insulators, quantum interferences, quantum transport, scattering

Received: January 31, 2020
Revised: April 11, 2020
Published online: June 2, 2020

[1] M. Z. Hasan, C. L. Kane, *Rev. Mod. Phys.* **2010**, *82*, 3045.
[2] X. L. Qi, S. C. Zhang, *Rev. Mod. Phys.* **2011**, *83*, 1057.
[3] Y. Ando, *J. Phys. Soc. Jpn.* **2013**, *82*, 102001.
[4] J. H. Bardarson, J. E. Moore, *Rep. Prog. Phys.* **2013**, *76*, 056601.
[5] H. Peng, K. Lai, D. Kong, S. Meister, Y. Chen, X. L. Qi, S. C. Zhang, Z. X. Shen, Y. Cui, *Nat. Mater.* **2010**, *9*, 225.
[6] J. G. Analytis, R. D. McDonald, S. C. Riggs, J. H. Chu, G. S. Boebinger, I. R. Fisher, *Nat. Phys.* **2010**, *6*, 960.
[7] J. H. Bardarson, P. W. Brouwer, J. E. Moore, *Phys. Rev. Lett.* **2010**, *105*, 156803.
[8] H. Steinberg, J. B. Laloe, V. Fatemi, J. S. Moodera, P. Jarillo-Herrero, *Phys. Rev. B* **2011**, *84*, 233101.
[9] B. Sacépé, J. B. Oostinga, J. Li, A. Ubaldini, N. J. Couto, E. Giannini, A. F. Morpurgo, *Nat. Commun.* **2011**, *2*, 575.
[10] F. Xiu, L. He, Y. Wang, L. Cheng, L. T. Chang, M. Lang, G. Huang, X. Kou, Y. Zhou, X. Jiang, Z. Chen, J. Zou, A. Shailos, K. L. Wang, *Nat. Nanotechnol.* **2011**, *6*, 216.
[11] J. Dufouleur, L. Veyrat, A. Teichgräber, S. Neuhaus, C. Nowka, S. Hampel, J. Cayssol, J. Schumann, B. Eichler, O. G. Schmidt, B. Büchner, R. Giraud, *Phys. Rev. Lett.* **2013**, *110*, 186806.
[12] S. S. Hong, Y. Zhang, J. J. Cha, X. L. Qi, Y. Cui, *Nano Lett.* **2014**, *14*, 2815.
[13] S. Cho, B. Dellabetta, R. Zhong, J. Schneeloch, T. Liu, G. Gu, M. J. Gilbert, N. Mason, *Nat. Commun.* **2015**, *6*, 7634.
[14] J. Dufouleur, L. Veyrat, B. Dassonneville, C. Nowka, S. Hampel, P. Leksin, B. Eichler, O. G. Schmidt, B. Büchner, R. Giraud, *Nano Lett.* **2016**, *16*, 6733.
[15] L. A. Jauregui, M. T. Pettes, L. P. Rokhinson, L. Shi, Y. P. Chen, *Nat. Nanotechnol.* **2016**, *11*, 345.
[16] V. E. Sacksteder, Q. Wu, *Phys. Rev. B* **2016**, *94*, 205424.
[17] J. Dufouleur, L. Veyrat, B. Dassonneville, E. Xypakis, J. H. Bardarson, C. Nowka, S. Hampel, J. Schumann, B. Eichler, O. G. Schmidt, B. Büchner, R. Giraud, *Sci. Rep.* **2017**, *7*, 45276.
[18] P. Seifert, K. Vaklinova, K. Kern, M. Burghard, A. Holleitner, *Nano Lett.* **2017**, *17*, 973.
[19] J. Dufouleur, E. Xypakis, B. Büchner, R. Giraud, J. H. Bardarson, *Phys. Rev. B* **2018**, *97*, 075401.
[20] R. Kozlovsky, A. Graf, D. Kochan, K. Richter, C. Gorini, *Phys. Rev. Lett.* **2020**, *124*, 126804.
[21] B. A. Bernevig, T. L. Hughes, S. C. Zhang, *Science* **2006**, *314*, 1757.
[22] X. L. Qi, S. C. Zhang, *Phys. Today* **2010**, *63*, 33.
[23] M. König, S. Wiedmann, C. Brüne, A. Roth, H. Buhmann, L. W. Molenkamp, X. L. Qi, S. C. Zhang, *Science* **2007**, *318*, 766.
[24] C. Kastl, C. Karnetzky, H. Karl, A. W. Holleitner, *Nat. Commun.* **2015**, *6*, 6617.
[25] J. Gooth, B. Hamdou, A. Dorn, R. Zierold, K. Nielsch, *Appl. Phys. Lett.* **2014**, *104*, 243115.
[26] R. Ilan, J. H. Bardarson, H. S. Sim, J. E. Moore, *New J. Phys.* **2014**, *16*, 053007.
[27] C. Nowka, L. Veyrat, S. Gorantla, U. Steiner, B. Eichler, O. G. Schmidt, H. Funke, J. Dufouleur, B. Büchner, R. Giraud, S. Hampel, *Cryst. Growth Des.* **2015**, *15*, 4272.

[28] J. Krieg, R. Giraud, H. Funke, J. Dufouleur, W. Escoffier, C. Trautmann, M. E. Toimil-Molares, *J. Phys. Chem. Solids* **2019**, *128*, 360.
[29] C. Jin, X. Xiang, C. Jia, W. Liu, W. Cai, L. Yao, X. Li, *J. Phys. Chem. B* **2004**, *108*, 1844.
[30] C. Frantz, N. Stein, Y. Zhang, E. Bouzy, O. Picht, M. E. Toimil-Molares, C. Boulanger, *Electrochim. Acta* **2012**, *69*, 30.
[31] J. Krieg, C. Chen, J. Avila, Z. Zhang, W. Sigle, H. Zhang, C. Trautmann, M. C. Asensio, M. E. Toimil-Molares, *Nano Lett.* **2016**, *16*, 4001.
[32] L. Veyrat, F. Iacovella, J. Dufouleur, C. Nowka, H. Funke, M. Yang, W. Escoffier, M. Goiran, B. Eichler, O. G. Schmidt, B. Büchner, S. Hampel, R. Giraud, *Nano Lett.* **2015**, *15*, 7503.
[33] S. Das Sarma, F. Stern, *Phys. Rev. B* **1985**, *32*, 8442.
[34] M. A. Paalanen, D. C. Tsui, J. C. M. Hwang, *Phys. Rev. Lett.* **1983**, *51*, 2226.
[35] P. T. Coleridge, R. Stoner, R. Fletcher, *Phys. Rev. B* **1989**, *39*, 1120.
[36] F. B. Mancoff, L. J. Zielinski, C. M. Marcus, K. Campman, A. C. Gossard, *Phys. Rev. B* **1996**, *53*, 7599.
[37] J. Tworzydlo, B. Trauzettel, M. Titov, A. Rycerz, C. W. J. Beenakker, *Phys. Rev. Lett.* **2006**, *96*, 246802.
[38] D. Culcer, E. H. Hwang, T. D. Stanescu, S. Das Sarma, *Phys. Rev. B* **2010**, *82*, 155457.
[39] D. Pesin, A. H. MacDonald, *Nat. Mater.* **2012**, *11*, 409.
[40] J. H. Bardarson, *J. Phys. A: Math. Theor.* **2008**, *41*, 405203.
[41] N. Tombros, A. Veligura, J. Junesch, M. H. D. Guimaraes, I. J. Vera-Marun, H. T. Jonkman, B. J. van Wees, *Nat. Phys.* **2011**, *7*, 697.
[42] B. Terrés, L. A. Chizhova, F. Libisch, J. Peiro, D. Jorger, S. Engels, A. Girschik, K. Watanabe, T. Taniguchi, S. V. Rotkin, J. Burgdorfer, C. Stampfer, *Nat. Commun.* **2016**, *7*, 11528.
[43] E. Akkermans, G. Montambaux, *Mesoscopic Physics of Electrons and Photons*, Cambridge University Press, Cambridge **2007**.
[44] A. E. Hansen, A. Kristensen, S. Pedersen, C. B. Sørensen, P. E. Lindelof, *Phys. Rev. B* **2001**, *64*, 045327.
[45] P. Roulleau, F. Portier, P. Roche, A. Cavanna, G. Faini, U. Gennser, D. Mailly, *Phys. Rev. Lett.* **2008**, *100*, 126802.
[46] Y. Xu, I. Miotkowski, C. Liu, J. Tian, H. Nam, N. Alidoust, J. Hu, C. K. Shih, M. Z. Hasan, Y. P. Chen, *Nat. Phys.* **2014**, *10*, 956.
[47] Y. Xu, I. Miotkowski, Y. P. Chen, *Nat. Commun.* **2016**, *7*, 11434.
[48] P. Schüffelgen, D. Rosenbach, C. Li, T. W. Schmitt, M. Schleenvoigt, A. R. Jalil, S. Schmitt, J. Kölzer, M. Wang, B. Bennemann, U. Parlak, L. Kibkalo, S. Trellenkamp, T. Grap, D. Meertens, M. Luysberg, G. Mussler, E. Berenschot, N. Tas, A. A. Golubov, A. Brinkman, T. Schäpers, D. Grützmacher, *Nat. Nanotechnol.* **2019**, *14*, 825.
[49] M. M. Otrokov, I. I. Klimovskikh, H. Bentmann, D. Estyunin, A. Zeugner, Z. S. Aliev, S. Gaß, A. U. B. Wolter, A. V. Koroleva, A. M. Shikin, M. Blanco-Rey, M. Hoffmann, I. P. Rusinov, A. Y. Vyazovskaya, S. V. Eremeev, Y. M. Koroteev, V. M. Kuznetsov, F. Freyse, J. Sánchez-Barriga, I. R. Amiraslanov, M. B. Babanly, N. T. Mamedov, N. A. Abdullayev, V. N. Zverev, A. Alfonsov, V. Kataev, B. Büchner, E. F. Schwier, S. Kumar, A. Kimura, et al., *Nature* **2019**, *576*, 416.
[50] E. D. L. Rienks, S. Wimmer, J. Sánchez-Barriga, O. Caha, P. S. Mandal, J. Růžička, A. Ney, H. Steiner, V. V. Volobuev, H. Groiss, M. Albu, G. Kothleitner, J. Michalička, S. A. Khan, J. Minár, H. Ebert, G. Bauer, F. Freyse, A. Varykhalov, O. Rader, G. Springholz, *Nature* **2019**, *576*, 423.
[51] A. Tan, V. Labracherie, N. Kunchur, A. U. B. Wolter, J. Cornejo, J. Dufouleur, B. Büchner, A. Isaeva, R. Giraud, *Phys. Rev. Lett.* **2020**, *124*, 197201.
[52] Y. Deng, Y. Yu, M. Z. Shi, Z. Guo, Z. Xu, J. Wang, X. H. Chen, Y. Zhang, *Science* **2020**, *367*, 895.
[53] S. Sykora, J. Schoop, L. Graf, G. Shipunov, I. V. Morozov, S. Aswartham, B. Büchner, C. Hess, R. Giraud, J. Dufouleur, arXiv:2002.01315v1 [cond-mat.mes-hall], **2020**.